FOR TABLE OF CONTENTS USE ONLY

High Throughput Synthesis and Screening of Oxygen Reduction Catalysts in the MTiO$_3$ (M = Ca, Sr, Ba) Perovskite Phase Diagram

Alexandra R. Groves[a], Thomas E. Ashton[a] and Jawwad A. Darr[a*]

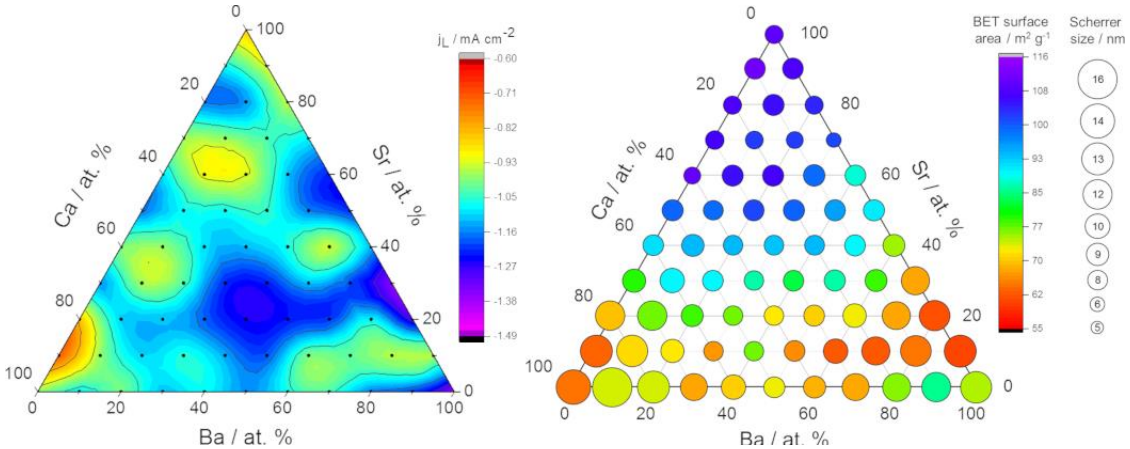

High Throughput Synthesis and Screening of Oxygen Reduction Catalysts in the $MTiO_3$ (M = Ca, Sr, Ba) Perovskite Phase Diagram

Alexandra R. Groves[a], Thomas E. Ashton[a] and Jawwad A. Darr[a*]

[a] *Department of Chemistry, University College London, 20 Gordon Street, Bloomsbury, London, WC1H 0AJ, U.K.*

*Corresponding author: Professor Jawwad A Darr.

Office telephone: +44 (0)20 7679 4345.

Research webpages http://www.ucl.me.uk.

Abstract

A library of 66 perovskite $Ba_xSr_yCa_zTiO_3$ ($x + y + z = 1$) samples (ca. three grams per sample) was made in ca. 14 hours using a high-throughput continuous hydrothermal flow synthesis system. The as-synthesised samples were collected from the outlet of the process and then cleaned and freeze dried before being evaluated individually as oxygen reduction catalysts using a rotating disk electrode testing technique. To establish any correlations between physical and electrochemical characterisation data, the as-synthesised samples were investigated using analytical methods including BET surface area, Powder X-ray Diffraction (PXRD) and in selected cases, Transmission Electron Microscopy (TEM). The aforementioned approach was validated as being able to quickly identify oxygen reduction catalysts from new libraries of electrocatalysts.

Key Words

Combinatorial synthesis, Continuous Hydrothermal Flow Synthesis, Green Chemistry, X-ray diffraction, Electrocatalysis, Oxygen reduction reaction

Introduction

The Oxygen Reduction Reaction (ORR) is of critical importance in the development of efficient energy storage and conversion devices such as metal-air batteries and low temperature fuel cells.[1] However, the ORR is widely recognised as the kinetic limiting component of these devices, often requiring a significant overpotential to reach a desirable current density,[2] and is therefore a major limiting factor in the application of an inexpensive, low temperature fuel cell.[3,4] Currently the most efficient and widely used catalyst for ORR is platinum.[5] However, *in operando* Pt is unstable and the dissolution, agglomeration and sintering of Pt nanoparticles during operation leads to an

overall reduction in electrochemical performance over time.[6] The scarcity and high cost of the platinum electrocatalysts are the largest contributing factor to the current high cost of fuel cells.[7,8] Therefore, it is desirable to develop a low cost electrocatalyst using earth abundant elements where possible.

Transition metal oxides have been extensively studied as ORR catalysts due to their relative high abundance, low cost and good thermal stability at the pH and potentials required for ORR.[9] In particular, perovskite heterometallic oxides (with the general structure ABO_3) have been explored as inexpensive ORR electrocatalysts as they fulfil the aforementioned requirements[10] and their intrinsic electrocatalytic activity can approach that of platinum, making then attractive in commercial applications.[11] Structurally, perovskite oxides offer huge versatility due to the large number of elements that can substituted into the '*A'* or '*B'* crystallographic sites leading to "tuneable activity".[9] A wide variety of perovskite mixed oxides have been studied as ORR catalysts, with those containing lanthanum at the '*A*' site receiving substantial interest.[12,13] In comparison, the use of perovskite barium titanate and its analogues as an ORR catalyst is relatively under explored.[14]

The synthesis of perovskites is traditionally carried out using co-precipitation or batch hydrothermal techniques, followed by a heat treatment step.[15,16] Alternatively, solid state "shake and bake" methods can be used, where high temperatures and multiple grinding steps are used to combat slow solid diffusion or insufficient precursor mixing.[17] This approach has a number of drawbacks; it uses multiple high energy processes and it yields poor size/shape control of particles, and materials can contain undesirable impurity phases.

Continuous hydrothermal processes for the production of nanopowders in flow, were first explored in the USA and in Japan in the 1990s.[18] More recently, the authors have developed variants of Continuous Hydrothermal Flow Synthesis (CHFS) processes that involve the production of nanoceramics using supercritical water. The CHFS process typically involves direct in-flow mixing of a combined flow of metal salt solution and base (ambient temperature, 240 bar) with a supercritical water flow (typically 450 °C, 240 bar) to produce nanoparticulate oxides at mixing temperatures in the range of ca. 280 - 400 °C. Previous CHFS studies showed the importance of mixer design (e.g. pipe diameters and geometries) and process conditions (precursor type, flow

rate, temperature, pressure, Reynolds number, etc.) on the final properties of the as-synthesised nanomaterials.[19–21]

The use of high throughput techniques to speed up materials discovery or optimisation is well established, with pharmaceutical industries being early adopters of the use of combinatorial synthetic techniques coupled to high throughput analysis methods.[22] In such approaches, many samples are made and screened to allow mapping of potential hotspots of activity. In inorganic nanomaterials combinatorial synthesis, there are challenges associated with comparing samples, due to the difficulty in making libraries under near-identical synthesis conditions. Several synthetic routes have been explored for the production of ORR active material libraries including thin film techniques that produce each composition on a milligram scale [23–25]. High throughput CHFS methods can also be used to produce large libraries of materials under consistent synthesis conditions (at the gram scale) in a matter of hours.[26–28] The use of high throughput CHFS to produce libraries of oxygen electrocatalysts is unreported until now.

In this report, the authors present the synthesis of a 66 sample library of potential ORR catalysts with the nominal composition $Ba_xSr_yCa_zTiO_3$ (x+y+z=1) that were produced sequentially via a high throughput CHFS based method; the powders made via this process were used as prepared and evaluated as ORR catalysts using a rotating disk electrode technique.

Experimental Procedures

Synthesis

Nano-sized alkaline earth metal titanate materials were synthesised using a Continuous Hydrothermal Flow Synthesis (CHFS) process (see fig. 1 for a schematic representation). The CHFS process pipework is built from standard 316 SS Swagelok™ parts (Swagelok Company, Hertfordshire, UK) and incorporates a patented co-current confined jet mixer (CJM, US Patent No. 20130136687), the design of which is described elsewhere.[29,30] A Ti sol was first synthesised by mixing Titanium(IV) Bis(Ammonium Lactate)Dihydroxide solution, TiBALD, 0.3 M, (Sigma-Aldrich, Dorset, UK, 50 wt. % in H_2O) with 0.09 M KOH (Fischer Scientific, Loughborough) inside a CHFS reactor (see Supporting Information for details). This Ti sol was the used without modification for the production of the target metal titanates. For the synthesis of the library, the required amounts of anhydrous $Ba(NO_3)_2$, anhydrous $Sr(NO_3)_2$ (Sigma Aldrich, Dorset, UK) and

$Ca(NO_3)_2.4H_2O$ (Sigma Aldrich, Dorset, UK) were dissolved into the Ti sol in appropriate molar ratios to create the 66 unique precursor solution recipes. The compositions as synthesised were based on the molecular weights as given by the manufacturer (exact precursor ratios can be found in the supporting information). Briefly, the CHFS process was as follows; three identical diaphragm pumps (Primeroyal K, Milton Roy, Point Saint-Pierre, France) were used to supply pressurised feeds at 24.1 MPa. Pump P1 (see P1, fig. 1) supplied deionised water at 80 mL min^{-1} (heated later in line), pump P2 (see P2, fig. 1) supplied 0.15 M metal salt/sol solutions (flow rate of 40 mL min^{-1}) and pump P3 (see P3, fig. 1) supplied 0.6 M potassium hydroxide (flow rate also 40 mL min^{-1}). The feeds from P2 and P3 were mixed in flow using a ¼ inch stainless steel T-piece. This combined flow was then mixed with supercritical water flow under turbulent conditions using a CJM, causing rapid precipitation of nanoparticles at a mixing temperature of ca. 335 °C. The resulting nanoparticulate slurry was cooled to ca. 40 °C using a pipe-in-pipe heat exchanger, before it exited the reactor via a Back-Pressure Regulator (BPR, TESCOM model 26-1762-24-194), which maintained a constant pressure in the system. The resulting nanoparticles were collected and centrifuged before being cleaned (dialysed until the water conductivity was <50 µS). The concentrated particle slurries were then each freeze-dried (Virtis Genesis 35XL) by heating the samples from −40 °C to 25 °C over 18 h under vacuum (range of 10 to 15 Pa). The freeze-dried powders were used as synthesised.

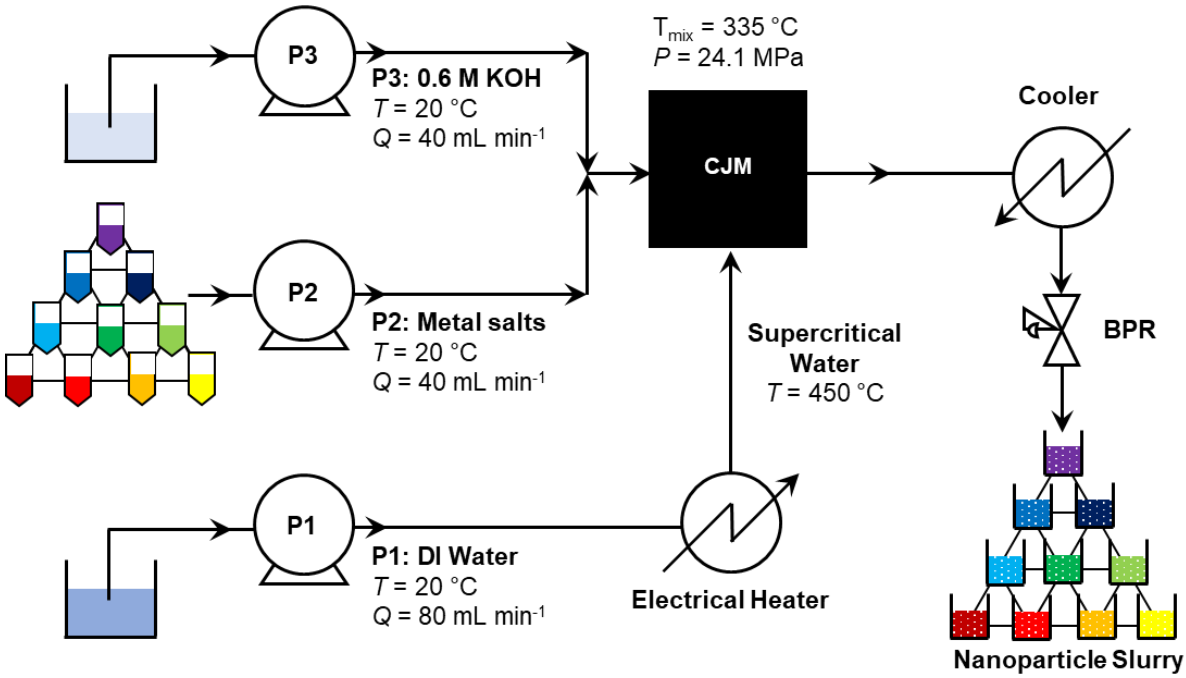

Figure 1: Process diagram for the production of the $Ba_xSr_yCa_zTiO_3$ 66 sample nanoparticle library of candidate ORR catalysts. P1 is pump 1, P2 is pump 2 and P3 is pump 3. BPR stands for back-pressure regulator and CJM stands for Confined Jet Mixer.

Physical characterisation

Powder X-ray diffraction (PXRD) was performed on a STOE StadiP diffractometer (STOE, Darmstadt, Germany) to collect diffraction patterns in a 2θ range of 2-40°, with a step size of 0.5°, and a step time of 15 s using Mo-Kα radiation (λ = 0.7093 Å).

Brauner-Emmett-Teller (BET) surface area measurements were carried out using a Micrometrics Tristar II (Micrometrics UK Ltd, Hertfordshire, UK) at the temperature of liquid nitrogen. The samples were degassed at 150 °C for 12 hr under N_2 before measurements were taken.

High-resolution transmission electron microscopy (TEM) was performed using a Jeol JEM 2100-LaB_6 filament (Joel, Hertfordshire, UK) was used to determine particle size and morphology. A small amount of material was sonicated in methanol until a uniform suspension was achieved. A Gatan Orius digital camera was used to capture images of the samples which were pipetted onto a 300 mesh copper film grid (Agar Scientific, Stansted, UK).

Electrochemical characterisation

The electrocatalytic activity for the ORR was studied with the Rotating Ring Disk Electrode (RRDE) technique using a PINE instruments rotator (PINE Research Instrumentation, Durham, USA, AFMSRCE) and a Gamry 1000 potentiostat (Gamry, Pennsylvania USA). The RRDE electrode consisted of a catalyst coated glassy carbon disk (geometric surface area = 0.25 cm^2) surrounded by a platinum ring (inner diameter 6.25 mm, outer diameter 7.92 mm). A three electrode RRDE cell (Adams Chittenden, Berkley, USA, model no. 946088) was used to carry out electrochemical measurements at room temperature. A platinum-wire (OD = 0.5 mm, Alfa Aesar, Lancashire, UK) was used as the counter electrode and a commercial Ag/AgCl electrode (BASi, Indiana, USA) was used as the reference. The electrolyte was 0.1 M NaOH solution prepared with deionised water and saturated with N_2 or O_2 (BOC, Guildford, UK) prior to each electrochemical measurement. The catalyst inks were made by mixing 5 mg as synthesised powder with 5 μL Nafion solution (5 wt% in water and lower aliphatic alcohols, Sigma Aldrich, Dorset, UK) and 2.5 mL of a 3:1 deionised water: isopropyl alcohol solution (Sigma Aldrich, Dorset, UK) in an

ultrasonic bath (VWR, USC100T) for 30 mins. The working electrode was prepared by spin coating 10 μL of the catalyst ink (using an old PINE instruments rotator model number above) onto the surface of the glassy carbon electrode and drying under an IR lamp for 15 mins.

Results and Discussion

The dried nanopowders were obtained with yields of >90% for all 66 samples. All materials were free flowing, white/-off white powders after washing and subsequent drying steps. These as-prepared powders were then used in the preparation of inks for use in the RDE experiments with no further treatments. XRF analysis was performed on the corners of the phase diagram to examine group 2 metal: titanium ratio. The actual Ba:Ti ratio was found to be 0.79:1, the ratio of Ca:Ti was found to be 0.89:1 and the ratio of Sr:Ti was found to be 0.80:1. The discrepancy between group 2 metal and Ti is likely due to the high solubility of Group 2 metal nitrate in solution leading to an excess of Ti in the final material. Nominal compositions are used to refer to all materials henceforth.

Phase identification:

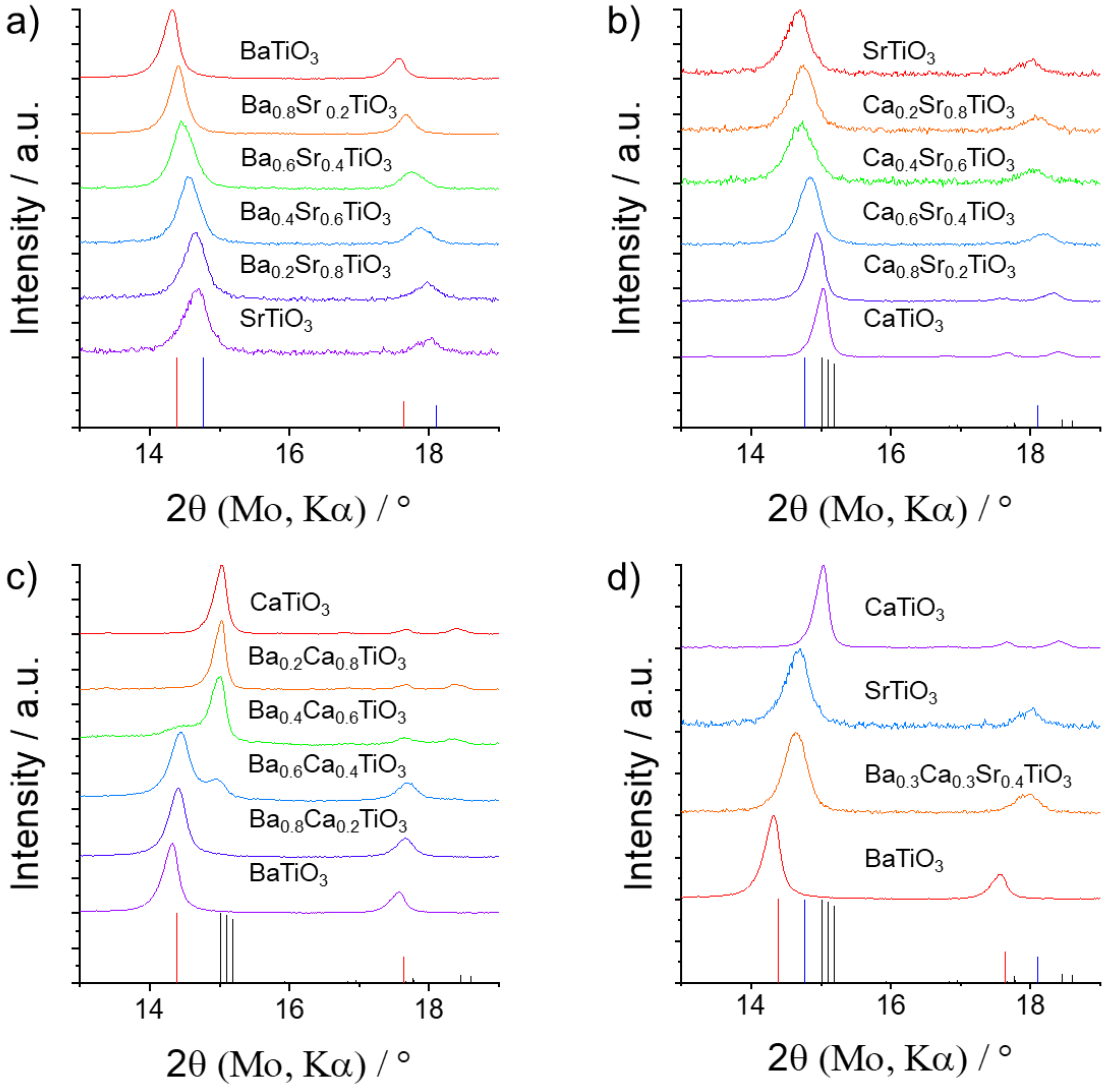

Figure 2: PXRD data of as synthesised materials from a selection of the structure plot. a) shows the PXRD data along the barium-strontium axis in steps of 0.2 atomic percent, b) shows the same along the strontium-calcium axis and c) along the barium-calcium axis. d) compositional effects the PXRD in the centre of the structure diagram compared to the corners. Red: $BaTiO_3$=ICSD collection code no. 80871[31], blue: $SrTiO_3$=ICSD collection code no. 71915[32] and black: $CaTiO_3$=ICSD collection code no. 67519[32].

The 66 samples were analysed using PXRD, which suggested that the materials were phase pure in all three corners of the phase diagram. The PXRD data for the binary barium-strontium titanate (fig. 2a) and the calcium-strontium titanate series (fig. 2b) suggests complete solid solutions formation across all compositions as expected from the relevant literature.[33] Analysis of the PXRD peak positions for the (110) peak revealed that peak position shifted from 12.5 to 12.8 degrees in 2θ for the Ba-$SrTiO_3$ series, and from 12.8 to 13.1 degrees in 2θ for the Sr-$CaTiO_3$ series. This is

in accordance with Vegards law where a change in ionic radii of the metal atom is expected to cause a linear change in lattice parameters, leading to a shift in observed peak position.[34]

In contrast to the two binary systems above, the barium-calcium titanate system revealed that a single perovskite phase was only observed up to ca. 20 at% Ca dopant in the Ba titanate structure and visa versa for the Ba in the Ca titanate (fig. 2c). At > 20 at% dopant levels, a separate calcium-titanate and a barium-titanate like phase, respective, co-existed with the solid solution. This is unsurprising given the large size mismatch between the Ba^{2+} and Ca^{2+} (ionic radius 1.61 and 1.34 Å respectively).[35] A report by Durst et al. suggested that a continuous solid solution can only be formed between elements of similar crystal structures, identical valency, similar electronegativity and only when solvent and solute atoms are of not too different sizes.[33] The percentage difference between the solute and solvent atoms must not exceed 15 %[36] for complete solid solution formation. In the case of Ca and Ba, the size factor difference is in the order of 20%.

In the centre of the compositional phase diagram, only a single perovskite phase was observed, suggesting that the presence of some Sr^{2+} ions supported the stabilisation of a solid solution, even when significant amounts of Ba^{2+} and Ca^{2+} were present. Overall, PXRD peaks were sharper at high Ba or Ca content, suggesting a larger primary particulate size. The results from Scherrer analysis on the (110) PXRD peak at ca. $2\theta = 14.5^{o}$ for all PXRD patterns are represented in fig. 3, below.

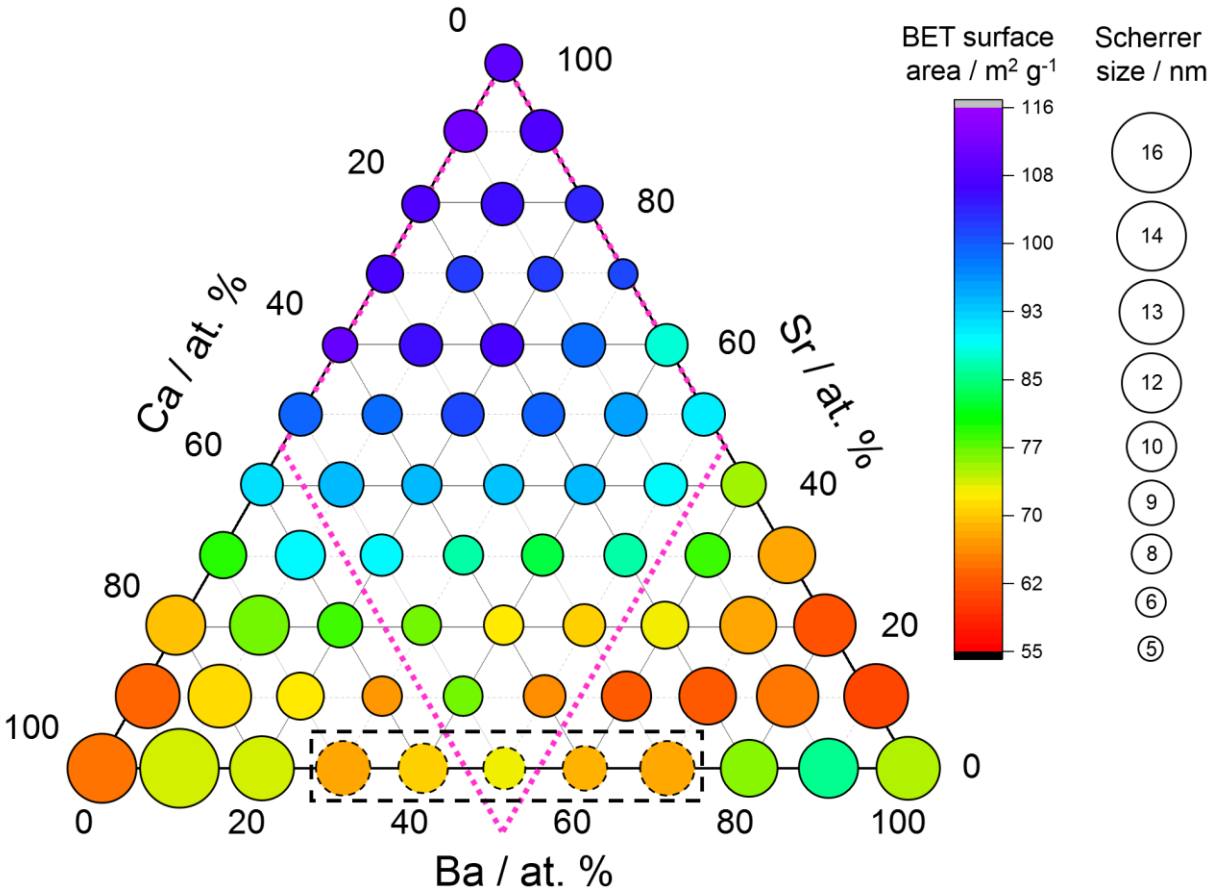

Figure 3: Physical characterization data for the full composition diagram. The size of each ball corresponds to the size calculated from the Scherrer equation. The colour of each ball corresponds to the BET surface area. Those balls with a black dashed line represent materials with a phase impurity seen in the XRD along the Ba-Ca titanate system. The pink dotted lines split the diagram roughly into three distinct areas of PXRD size.

The dividing pink lines on the diagram highlight three approximate regions separated by Scherrer size (crystallite domain size), calculated assuming spherical particles for all materials. Those within the pink dotted diamond (low Ba / low Ca) are in the size range of 5 to 11 nm, whereas those in the triangular areas (high Ba/ high Ca) are larger, in the size range of 12 to 16 nm. Only five materials had a dual phase present according to the PXRD (fig. 3, black dashed box) due to the miscibility gap, resulting from the size mismatch between Ba and Ca in the titanate (as discussed earlier).

BET surface area measurements were carried out on all 66 materials with specific surface areas (SSA) in the range 54 to 116 m^2 g^{-1} (see fig. 3). The full table of values can be found in the Supporting Information. The surface area in or around the corners of the composition diagram

were consistently higher than samples of group 2 titanates reported previously in the literature (8.5 $m^2\ g^{-1}$ for $BaTiO_3$ to 75 for $SrTiO_3$ $m^2\ g^{-1}$),[37–39] which is attributed to the relatively mild synthesis conditions. The BET data reveals that samples containing high at% Sr and Ca had the highest and lowest surface areas respectively. The full list of physical characterisation data can be found in the supporting information (table S2).

TEM images (fig. 4) of the single metal titanates revealed that the size and shape of the individual titanates varied greatly depending on the composition. Samples containing higher at% of Ca had large differences in particle size and shape, suggesting Ostwald ripening of small particles into larger ones occurred to a greater extent. Cubes, rods and small circular particles were seen. However, materials high in Sr and Ba were largely irregular circular particles. This may have explained the slight discrepancies between the trends in Scherrer size and expected BET surface area, as those materials containing significant amounts of calcium may have significantly different surface area to volume ratios to the rest of the compositions.

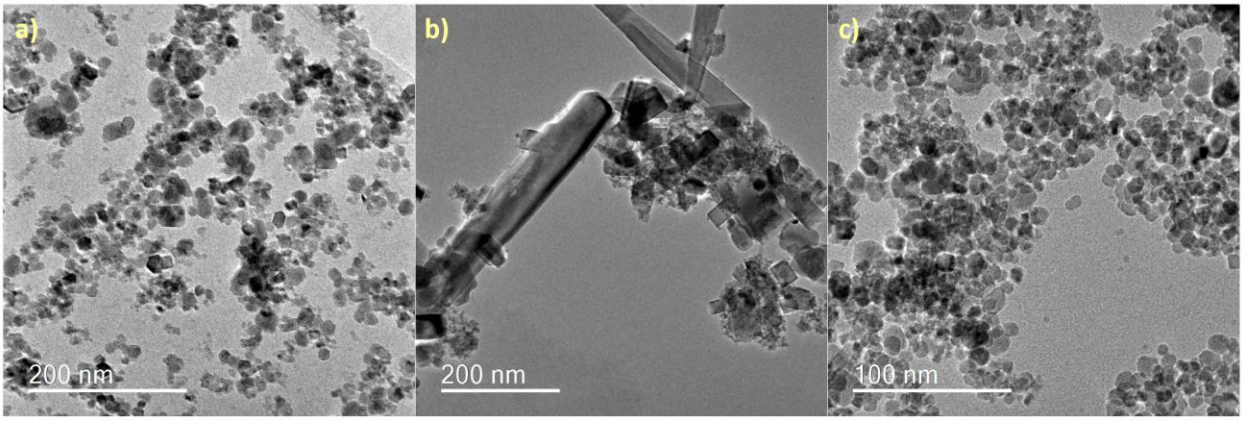

Figure 4: Transmission electron microscope images of as synthesised materials: a) $BaTiO_3$, b) $CaTiO_3$ and c) $SrTiO_3$

Electrochemical Characterisation:

Initial electrochemical screening was undertaken using a Rotating Disk Electrode (RDE) and samples could be electrochemically screened in ca. 10 minutes each. Identical amounts (0.08 mg cm^{-2}) of the as-prepared nanopowder catalyst was loaded onto a Glassy Carbon (GC) RDE which was then placed into an electrochemical cell containing O_2 saturated 0.1 M NaOH. The catalyst layer was first pacified and then the disk was rotated at 4 speeds (400, 900, 1600 and 2500) and linear sweep voltammograms collected at 10 mV s^{-1}. The current density was recorded at a fixed

potential of −0.5 V and a rotation speed of 900 rpm so that a comparison between all catalysts could be recorded. Current densities were calculated in relation to the geometric surface area of the RDE. Fig. 5) shows the typical voltammogram response seen by all the catalysts. The spacing between the current responses seen at different rotation speeds is related to the square of the rotation speed in line with the Kouteky-Levich equation.

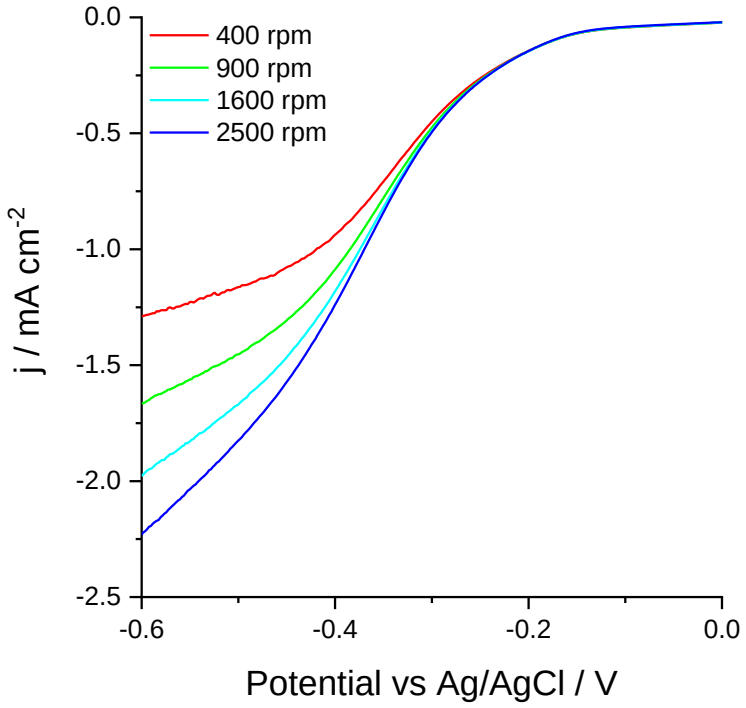

Figure 5: Current vs voltage responses of the $BaTiO_3$ catalyst at four different rotation speeds.

Fig. 6a) shows the variation seen in current density (taken at −0.5 V vs Ag/AgCl and 900 rpm) with composition. Values for all samples can be found in the Supplimentary information. It can be seen that the current density achieved was composition dependent; samples with high Ba content had more negative limiting current denisties than catalysts containing high Ca content, making those materials high in Ba better ORR catalysts. This suggests that the activity of the catalyats towards the ORR is directly related to the alkaline earth metal used in the A site. By comparing the SSA diagram to fig. 6a) it seems to suggest that an intermediate SSA is favoured for the ORR in this case.

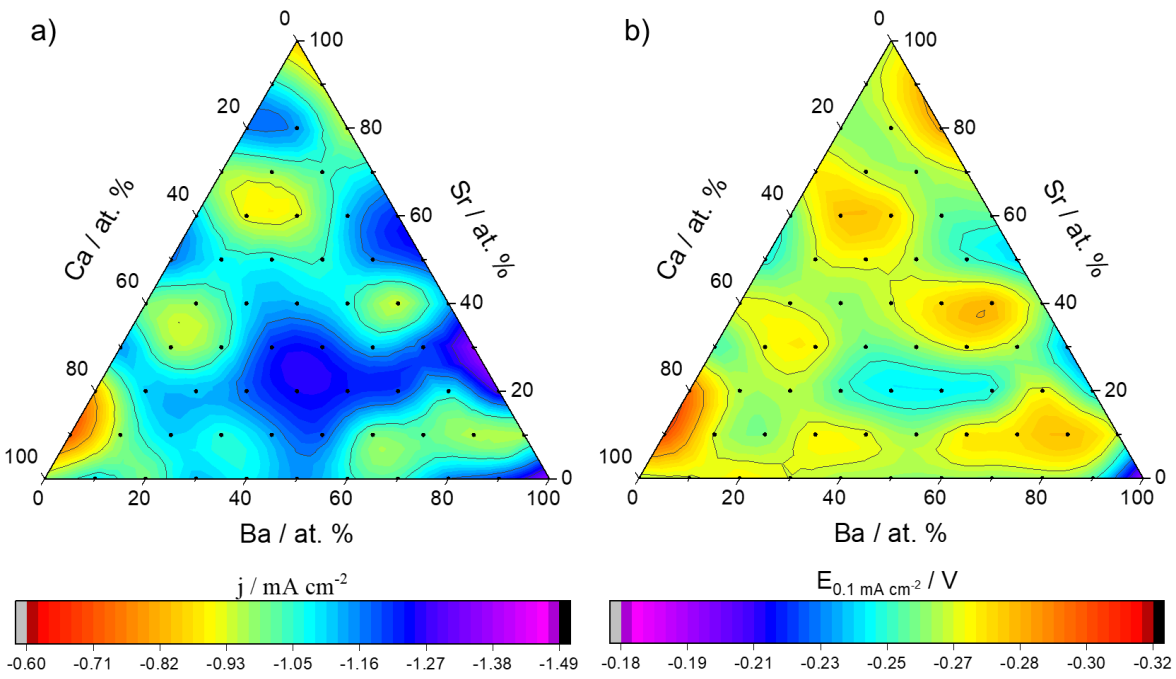

Figure 6: a) Limiting current density taken at −0.5 V vs Ag/AgCl, b) Onset potential taken at a current density of −0.1 mA cm^{-2}. All data has been taken in O_2 saturated 0.1 M NaOH electrolyte at 900 rpm.

Fig. 6b) shows the onset potential of the ORR and has been taken when the current density reached −0.1 mA cm^{-2}. The difference in onset potential shows less variety than the difference in current densities, with only samples at the corners of the triangular phase diagram showing significant variation. Both onset potential and current density are poor in the left-hand corner corresponding to high calcium content in the material. In direct comparison, the best performance is seen in the right-hand corner for both catalytic markers corresponding to high barium content.

The best electrocatalyst highlighted from the combinatorial study was $Ba_{0.8}Sr_{0.2}TiO_3$ with a high limiting current reached of −1.49 mA cm^{-2} at 900 rpm and a low onset potential of −0.2 V vs Ag/AgCl. To the authors knowledge this composition has never been reported as an ORR catalyst in the literature before. Comparing to h-$BaTiO_3$ reported by Chen *et al*., the onset potential reported herein for $BaTiO_3$ (0.84 V vs RHE) is shifted to a more positive value than previously reported (0.82 V vs RHE).[14] This suggests that the CHFS synthetic route is a suitable method for the high through put synthesis of groups of transition metal catalysts to screen for areas of catalytic activity, as results are more positive than previously reported with no optimisation of synthetic conditions.

Conclusions

A 66 sample library of Ca-Sr-Ba titanate perovskite nanoparticles was rapidly and consistently manufactured using a direct continuous hydrothermal synthesis approach. All the materials had the perovskite structure ($SrTiO_3$ and $BaTiO_3$-Cubic, $CaTiO_3$ orthorhombic) although those along the binary $Ca_xBa_{1-x}TiO_3$ line, the co-existence of two perovskite solid solution phases was observed above 25 at% dopant (as expected) due to the large size mismatch between Ca^{2+} and Ba^{2+} ions. Due to the nature of the rapid hydrothermal synthesis method, the BET surface area measurements for the as-prepared catalysts were approximately 40 $m^2\ g^{-1}$ higher than similar materials reported in the literature previously (that were made by solid state methods).

Initial electrochemical screening for ORR electrocatalytic activity, revealed that materials high in Ba and low in Sr content had high electrocatalytic activity. In particular, sample $Ba_{0.8}Sr_{0.2}TiO_3$ had a high current response for the ORR paired with a low onset potential. Overall, the samples in the library had gradual changes in properties, which further suggested that the CHFS routes offered a consistent method of manufacture which in turn facilitated comparison between the electrochemical and analytical data of the potential ORR catalysts. High throughput CHFS has proven to be a rapid and efficient method of synthesising libraries of materials to identify candidates for the electrocatalytic reduction of oxygen.

Author Information

Corresponding Author: * Email: j.a.darr@ucl.ac.uk. **Author Contributions:** A.R.G. and J.A.D. designed the synthesis, T.E.A. performed the synthesis with A.R.G, A.R.G. performed all experiments and A.R.G. wrote the manuscript and Supporting Information. **Conflict of Interest:** The authors declare no conflict of interest

Acknowledgements

The Juiced energy hub is thanked for supporting JAD (EP/R023662/1 ISCF Wave 1: (The JUICED Hub [Joint University Industry Consortium for Energy (Materials) and Devices Hub]) and the EPSRC is thanked for supporting a studentship for ARG.

References

(1) Debe, M. K. Electrocatalyst Approaches and Challenges for Automotive Fuel Cells. *Nature* **2012**, *486* (7401), 43–51. https://doi.org/10.1021/acs.jpcc.5b08761.

(2) Ge, X.; Sumboja, A.; Wuu, D.; An, T.; Li, B.; Goh, F. W. T.; Hor, T. S. A.; Zong, Y.; Liu, Z. Oxygen Reduction in Alkaline Media: From Mechanisms to Recent Advances of Catalysts. *ACS Catal.* **2015**, *5* (8), 4643–4667. https://doi.org/10.1021/acscatal.5b00524.

(3) Chen, Z.; Higgins, D.; Yu, A.; Zhang, L.; Zhang, J. A Review on Non-Precious Metal Electrocatalysts for PEM Fuel Cells. *Energy Environ. Sci.* **2011**, *4* (9), 3167–3192. https://doi.org/10.1039/c0ee00558d.

(4) Atta, N. F.; Galal, A.; El-Ads, E. H. *Perovskite Nanomaterials – Synthesis, Characterization, and Applications*; Pan, L., Zhu, G., Eds.; IntechOpen, 2016. https://doi.org/10.5772/61280.

(5) Tarasevich, M. R.; Korchagin, O. V. Electrocatalysis and PH (a Review). *Russ. J. Electrochem.* **2013**, *49* (7), 600–618. https://doi.org/10.1134/S102319351307015X.

(6) Hwang, J.; Rao, R. R.; Giordano, L.; Katayama, Y.; Yu, Y.; Shao-Horn, Y. Perovskites in Catalysis and Electrocatalysis. *Science (80-.).* **2017**, *358* (6364), 751–756. https://doi.org/10.1126/science.aam7092.

(7) Wang, Y.; Chen, K. S.; Mishler, J.; Cho, S. C.; Adroher, X. C. A Review of Polymer Electrolyte Membrane Fuel Cells: Technology, Applications and Needs on Fundamental Research. *J. Mater. Sci.* **2000**, *35* (19), 4857–4863. https://doi.org/10.1016/j.apenergy.2010.09.030.

(8) Steele, B. C. H.; Heinzel, A. Materials for Fuel-Cell Technologies. *Nature* **2001**, *414* (November), 345–352.

(9) Hayden, B. E.; Rogers, F. K. Oxygen Reduction and Oxygen Evolution on SrTi1 − XFexO3 − y(STFO) Perovskite Electrocatalysts. *J. Electroanal. Chem.* **2018**, *819* (July 2017), 275–282. https://doi.org/10.1016/j.jelechem.2017.10.056.

(10) Hong, W. T.; Risch, M.; Stoerzinger, K. A.; Grimaud, A.; Suntivich, J.; Shao-Horn, Y.

Toward the Rational Design of Non-Precious Transition Metal Oxides for Oxygen Electrocatalysis. *Energy Environ. Sci.* **2015**, *8* (5), 1404–1427. https://doi.org/10.1039/C4EE03869J.

(11) Lee, Y.; Suntivich, J.; May, K. J.; Perry, E. E.; Shao-Horn, Y. Synthesis and Activities of Rutile IrO 2 and RuO 2 Nanoparticles for Oxygen Evolution in Acid and Alkaline Solutions. *J. Phys. Chem. Lett.* **2012**, *3* (3), 399–404. https://doi.org/10.1021/jz2016507.

(12) Zhou, S.; Miao, X.; Zhao, X.; Ma, C.; Qiu, Y.; Hu, Z.; Zhao, J.; Shi, L.; Zeng, J. Engineering Electrocatalytic Activity in Nanosized Perovskite Cobaltite through Surface Spin-State Transition. *Nat. Commun.* **2016**, *7* (May), 1–7. https://doi.org/10.1038/ncomms11510.

(13) Bockris, J. O. The Electrocatalysis of Oxygen Evolution on Perovskites. *J. Electrochem. Soc.* **1984**, *131* (2), 290. https://doi.org/10.1149/1.2115565.

(14) Chen, C. F.; King, G.; Dickerson, R. M.; Papin, P. A.; Gupta, S.; Kellogg, W. R.; Wu, G. Oxygen-Deficient BaTiO3-Xperovskite as an Efficient Bifunctional Oxygen Electrocatalyst. *Nano Energy* **2015**, *13*, 423–432. https://doi.org/10.1016/j.nanoen.2015.03.005.

(15) Hayashi, H.; Hakuta, Y. Hydrothermal Synthesis of Metal Oxide Nanoparticles in Supercritical Water. *Materials (Basel).* **2010**, *3* (7), 3794–3817. https://doi.org/10.3390/ma3073794.

(16) Ecija, A.; Vidal, K.; Larrañaga, A.; Ortega San Martin, L.; Arriortua, M. I.; Larraaga, A.; Ortega-San-Martn, L.; Isabel, M. Synthethic Methods for Perovskite Materials: Structure and Morphology. *Adv. Cryst. Process.* **2012**, 485–506. https://doi.org/10.1002/anie.201305368.

(17) Fukuoka, H.; Isami, T.; Yamanaka, S. Superconductivity of Alkali Metal Intercalated Niobate with a Layered Perovskite Structure. *Chemistry Letters*. 1997, pp 703–704. https://doi.org/Doi 10.1246/Cl.1997.703.

(18) Adschiri, T.; Kanazawa, K.; Arai, K. Rapid and Continuous Hydrothermal Crystallization of Metal Oxide Particles in Supercritical Water. *J. Am. Ceram. Soc.* **1992**, *75* (4), 1019–

1022. https://doi.org/10.1111/j.1151-2916.1992.tb04179.x.

(19) Powell, M. J.; Marchand, P.; Denis, C. J.; Bear, J. C.; Darr, J. A.; Parkin, I. P. Direct and Continuous Synthesis of VO 2 Nanoparticles. *Nanoscale* **2015**, *7* (44), 18686–18693. https://doi.org/10.1039/C5NR04444H.

(20) Lester, E.; Aksomaityte, G.; Li, J.; Gomez, S.; Gonzalez-Gonzalez, J.; Poliakoff, M. Controlled Continuous Hydrothermal Synthesis of Cobalt Oxide (Co3O4) Nanoparticles. *Prog. Cryst. Growth Charact. Mater.* **2012**, *58* (1), 3–13. https://doi.org/10.1016/j.pcrysgrow.2011.10.008.

(21) Darr, J. A.; Zhang, J.; Makwana, N. M.; Weng, X. Continuous Hydrothermal Synthesis of Inorganic Nanoparticles: Applications and Future Directions. *Chem. Rev.* **2017**, *117*, 11125–11238. https://doi.org/10.1021/acs.chemrev.6b00417.

(22) Chighine, A.; Sechi, G.; Bradley, M. Tools for Efficient High-Throughput Synthesis. *Drug Discov. Today* **2007**, *12* (11–12), 459–464. https://doi.org/10.1016/j.drudis.2007.04.004.

(23) Guerin, S.; Hayden, B. E.; Lee, C. E.; Mormiche, C.; Russell, A. E. High-Throughput Synthesis and Screening of Ternary Metal Alloys for Electrocatalysis. *J. Phys. Chem. B* **2006**, *110* (29), 14355–14362. https://doi.org/10.1021/jp061967d.

(24) Schäfer, D.; Mardare, C.; Savan, A.; Sanchez, M. D.; Mei, B.; Xia, W.; Muhler, M.; Ludwig, A.; Schuhmann, W. High-Throughput Characterization of Pt Supported on Thin Film Oxide Material Libraries Applied in the Oxygen Reduction Reaction. *Anal. Chem.* **2011**, *83* (6), 1916–1923. https://doi.org/10.1021/ac102303u.

(25) Park, S. H.; Choi, C. H.; Koh, J. K.; Pak, C.; Jin, S. A.; Woo, S. I. Combinatorial High-Throughput Screening for Highly Active Pd-Ir-Ce Based Ternary Catalysts in Electrochemical Oxygen Reduction Reaction. *ACS Comb. Sci.* **2013**, *15* (11), 572–579. https://doi.org/10.1021/co400008v.

(26) Weng, X.; Cockcroft, J. K.; Hyett, G.; Vickers, M.; Boldrin, P.; Tang, C. C.; Thompson, S. P.; Parker, J. E.; Knowles, J. C.; Rehman, I.; Parkin, I.; Evans, J. R. G.; Darr, J. A. High-Throughput Continuous Hydrothermal Synthesis of an Entire Nanoceramic Phase

Diagram. *J. Comb. Chem.* **2009**, *11* (5), 829–834. https://doi.org/10.1021/cc900041a.

(27) Quesada-Cabrera, R.; Weng, X.; Hyett, G.; Clark, R. J. H.; Wang, X. Z.; Darr, J. A. High-Throughput Continuous Hydrothermal Synthesis of Nanomaterials (Part II): Unveiling the as-Prepared CexZryYzO 2-δ Phase Diagram. *ACS Comb. Sci.* **2013**, *15* (9), 458–463. https://doi.org/10.1021/co3001346.

(28) Marchand, P.; Makwana, N. M.; Tighe, C. J.; Gruar, R. I.; Parkin, I. P.; Carmalt, C. J.; Darr, J. A. High-Throughput Synthesis, Screening, and Scale-Up of Optimized Conducting Indium Tin Oxides. *ACS Comb. Sci.* **2016**, *18* (2), 130–137. https://doi.org/10.1021/acscombsci.5b00166.

(29) Gruar, R. I.; Tighe, C. J.; Southern, P.; Pankhurst, Q. A.; Darr, J. A. A Direct and Continuous Supercritical Water Process for the Synthesis of Surface-Functionalized Nanoparticles. *Ind. Eng. Chem. Res.* **2015**, *54* (30), 7436–7451. https://doi.org/10.1021/acs.iecr.5b01817.

(30) Gruar, R. I.; Tighe, C. J.; Darr, J. A. Scaling-up a Confined Jet Reactor for the Continuous Hydrothermal Manufacture of Nanomaterials. *Ind. Eng. Chem. Res.* **2013**, *52* (15), 5270–5281. https://doi.org/10.1021/ie302567d.

(31) Abramov, Y. A.; Tsirelson, V. G.; Zavodnik, V. E.; Ivanov, S. A.; Brown, I. D. The Chemical Bond and Atomic Displacements in SrTiO3 from X-ray Diffraction Analysis. *Acta Crystallogr. Sect. B* **1995**, *51* (6), 942–951. https://doi.org/10.1107/S0108768195003752.

(32) Buttner, R. H.; Maslen, E. N. Electron Difference Density and Structural Parameters in CaTiO3. *Acta Crystallogr. Sect. B* **1992**, *48* (5), 644–649. https://doi.org/10.1107/S0108768192004592.

(33) Durst, G.; Grotenhuis, M.; Barkow, A. G. Solid Solubility Study of Barium, Strontium, and Calcium Titanates. *J. Am. Ceram. Soc.* **1950**, *33* (4), 133–139. https://doi.org/10.1111/j.1151-2916.1950.tb12775.x.

(34) Vegard, von L. Der Mischkristalle Unde Die Raumfullung Der Atome. *Zeitschrift für Phys.* **1921**, *5* (1), 17–26.

(35) Shannon, R. D. Revised Effective Ionic Radii in Halides and Chalcogenides. *Acta Cryst. A* **1976**, *32* (5), 751–767. https://doi.org/10.1107/S0567739476001551.

(36) Hume-rothery, A. W.; Mabbott, G. W.; Evans, K. M. C. The Freezing Points, Melting Points, and Solid Solubility Limits of the Alloys of Silver, and Copper with the Elements of the B Sub-Groups. *Philos. Trans. A. Math. Phys. Eng. Sci.* **1934**, *233*, 1–97.

(37) Pfaff, G. Synthesis of Calcium Titanate Powders by the Sol-Gel Process. *Chem. Mater.* **1994**, *6* (1), 58–62. https://doi.org/10.1021/cm00037a013.

(38) Uchino, K.; Sadanaga, E.; Hirose, T. Dependence of the Crystal Structure on Particle Size in Barium Titanate. *J. Am. Ceram. Soc.* **1989**, *72* (8), 1555–1558. https://doi.org/10.1111/j.1151-2916.1989.tb07706.x.

(39) Burnside, S.; Moser, J.-E.; Brooks, K.; Grätzel, M.; Cahen, D. Nanocrystalline Mesoporous Strontium Titanate as Photoelectrode Material for Photosensitized Solar Devices: Increasing Photovoltage through Flatband Potential Engineering. *J. Phys. Chem. B* **1999**, *103* (43), 9328–9332. https://doi.org/10.1021/jp9913867.

Supporting Information

Complete synthetic details and tables of results for all samples can be found in the Supporting Information.